

Comparison of various methods to extract ringdown frequency from gravitational wave data

Hiroyuki Nakano,^{1,*} Tatsuya Narikawa,^{2,3,†} Ken-ichi Oohara,^{4,‡} Kazuki Sakai,^{5,§}
Hisaki Shinkai,^{6,||} Hirotaka Takahashi,^{7,8,¶} Takahiro Tanaka,^{3,9,**} Nami Uchikata,^{2,4,††}
Shun Yamamoto,⁶ and Takahiro S. Yamamoto^{3,‡‡}

¹*Faculty of Law, Ryukoku University, Kyoto 612-8577, Japan*

²*Institute for Cosmic Ray Research, The University of Tokyo, Chiba 277-8582, Japan*

³*Department of Physics, Kyoto University, Kyoto 606-8502, Japan*

⁴*Graduate School of Science and Technology, Niigata University, Niigata 950-2181, Japan*

⁵*Department of Electronic Control Engineering, National Institute of Technology, Nagaoka College, Niigata 940-8532, Japan*

⁶*Faculty of Information Science and Technology, Osaka Institute of Technology, Kitayama, Hirakata City, Osaka 573-0196, Japan*

⁷*Department of Information and Management Systems Engineering, Nagaoka University of Technology, Niigata 940-2188, Japan*

⁸*Earthquake Research Institute, The University of Tokyo, Tokyo 113-0032, Japan*

⁹*Center for Gravitational Physics, Yukawa Institute for Theoretical Physics, Kyoto University, Kyoto 606-8502, Japan*



(Received 16 November 2018; published 21 June 2019)

The ringdown part of gravitational waves in the final stage of the merger of compact objects tells us the nature of strong gravity and hence can be used for testing theories of gravity. The ringdown waveform, however, fades out in a very short time with a few cycles, and hence it is challenging to extract the ringdown frequency and its damping timescale. We here propose to build up a suite of mock data of gravitational waves to compare the performance of various approaches developed to detect the dominant quasinormal mode from an excited black hole after merger. In this paper, we present our initial results of comparisons of the following five methods: (1) plain matched filtering with ringdown part method, (2) matched filtering with both merger and ringdown parts method, (3) Hilbert-Huang transformation method, (4) autoregressive modeling method, and (5) neural network method. After comparing the performances of these methods, we discuss our future projects.

DOI: [10.1103/PhysRevD.99.124032](https://doi.org/10.1103/PhysRevD.99.124032)

I. INTRODUCTION

Both in the year 2016 and 2017, the physics community was very excited by the reports of direct detections of gravitational waves (GWs) by the LIGO and Virgo Collaborations [1–6]. The direct detections definitely prove the correctness of the fundamental idea of general relativity (GR), together with that of the direction of efforts of theoretical and experimental research of gravity.

The LIGO and Virgo Collaborations have so far performed their observations twice [observing runs 1 (O1), September 12, 2015–January 19, 2016 (48.6 days) and O2, November 30, 2016–August 25, 2017 (118 days)] and officially reported [7,8] that they detected 11 events: ten binary black hole (BH) events and one event of the merger of binary neutron stars (GW170817 [6]). Both types of sources gave us certain advances not only to physics, but also to astrophysics.

In late 2019, another ground-based GW detector, KAGRA, will join the network of GW observation [9–11]. This will make the source localization more precise, and we also expect to detect the polarization of GWs for each event. By accumulating observations, we will be able to investigate new aspects of physics and astronomy, such as the distribution of binary parameters, formation history of binaries, equation of state of the nuclear matter, and cosmological parameters.

Among such possibilities, our interest lies in testing various gravity theories. GR has passed all the tests in the past century, and nobody doubts gravity is basically

*hinakano@law.ryukoku.ac.jp

†narikawa@tap.scphys.kyoto-u.ac.jp

‡oohara@astro.sc.niigata-u.ac.jp

§k-sakai@nagaoka-ct.ac.jp

||hisaaki.shinkai@oit.ac.jp

¶hirotaka@kjs.nagaokaut.ac.jp

**t.tanaka@tap.scphys.kyoto-u.ac.jp

††uchikata@astro.sc.niigata-u.ac.jp

‡‡yamamoto@tap.scphys.kyoto-u.ac.jp

described by GR. However, almost of the tests so far have been performed in the weak gravity regime (tests around the Earth, in the Solar System, or using binary pulsars) [12], and we still require tests in the strong gravity regime, which is relevant to describe, say, BH mergers. Observations of GWs from binary BHs will enable us to test the gravity theories in this extreme regime.

The previous detections of BH mergers have shown that the inspiral phase (premerger phase) is well described by post-Newtonian approximation. But it is not entirely clear whether or not the ringdown phase (postmerger phase), which is expected to be well described by BH perturbation theory, was detected in the GW data. This is because identifying ringdown modes of a BH from noisy data is a quite challenging task for data analysis. Ringdown modes decay quite rapidly for a typical BH described by GR. For example, for a typical BH formed after merger with the total mass $M = 60M_\odot$ and the angular momentum (normalized Kerr parameter) $\chi = 0.75$, the dominant ringdown mode ($\ell = m = 2$) has the characteristic frequency $f_R = 300$ Hz and the damping time $\tau = 3.7$ msec, which indicates that the amplitude is reduced to about 40% after one cycle of oscillation.

One way to give clear evidence of detection of the ringdown mode would be just to improve the detector sensitivity. However, it will also give a similar impact if we can improve the significance of detection by implementing an optimized data analysis method. There have already been several technical proposals of methods to identify the ringdown mode (see, e.g., Refs. [13–16] or reviews, e.g., Refs. [17,18]), but we think that a fair comparison of the performance of different methods has not been presented yet. To find the optimal method, we organize mock-data tests. The idea is to extract the information of the ringdown part [its frequency f_R and damping time τ (imaginary part of frequency f_I or quality factor Q)] independent of the other parts of the waveform. In order not to allow identification of the properties of mergers from the inspiral waveform using relations valid in GR, we prepare a set of blind data, each of which has a randomly chosen f_R and f_I different from the GR predicted value (see Sec. II A).

In general, the ringdown part includes not only the dominant mode but also subdominant modes. The analysis of various modes (BH spectroscopy) is also important for tests of gravity theories (e.g., Ref. [19]). However, the amplitudes of these subdominant modes are small compared with one of the dominant mode [16]. Thus, in this work, we focus on the case existing with only a single mode.

We present our comparisons of the following five methods: (1) matched filtering with ringdown part (MF-R), (2) matched filtering with both merger and ringdown parts (MF-MR), (3) Hilbert-Huang transformation (HHT), (4) autoregressive modeling (AR), and (5) neural network (NN). Each method will be explained separately in Sec. III.

In Sec. IV, we compare the results together with future directions for improvement and we also discuss some issues for application to the real data. The mock data we use in this article are available from our web page [20].

II. BUILDING MOCK DATA

A. Quasinormal modes

The waveform of the ringdown gravitational waves emitted from an excited BH is modeled as

$$h(t) = Ae^{-(t-t_0)/\tau} \cos(2\pi f_R(t-t_0) - \phi_0), \quad (2.1)$$

where f_R is the oscillation frequency, τ is the damping time, and t_0 and ϕ_0 are the initial time and its phase, respectively. The waveform (2.1) is then written as

$$h(t) = \Re[Ae^{-2\pi i f_{\text{qnm}}(t-t_0)}], \quad (2.2)$$

where we call $f_{\text{qnm}} = f_R - if_I$ the quasinormal mode (QNM, or ringdown) frequency ($f_I > 0$ means decaying mode). (Nakano *et al.* [21] use a different signature on f_I .) The parameter τ is also expressed using a quality factor Q or f_I

$$Q = \pi f_R \tau \quad \text{or} \quad f_I = \frac{1}{2\pi\tau} = \frac{f_R}{2Q}. \quad (2.3)$$

In GR, the set of (f_R, f_I) is determined by the (remnant BH) mass M_{rem} and angular momentum $M_{\text{rem}}^2 \chi$ of the black hole. QNM is obtained from the perturbation analysis of BHs, and its fitting formulas are given by [22]

$$f_R = \frac{1}{2\pi M_{\text{rem}}} \{f_1 + f_2(1-\chi)^{f_3}\}, \quad (2.4)$$

$$Q = \frac{f_R}{2f_I} = q_1 + q_2(1-\chi)^{q_3}, \quad (2.5)$$

where f_i and q_i are the fitting coefficients. For the most fundamental mode, which is of the spherical harmonic index $\ell = 2$, $m = 2$, the fitting parameters are $f_1 = 1.5251$, $f_2 = -1.1568$, $f_3 = 0.1292$, $q_1 = 0.7000$, $q_2 = 1.4187$, and $q_3 = -0.4990$.

If we recover the units,

$$f_R(M, \chi)[\text{Hz}] = \frac{c^3}{2\pi G M_{\text{rem}}} \{f_1 + f_2(1-\chi)^{f_3}\}, \quad (2.6)$$

where c and G are the speed of light and the gravitational constant, respectively. From this equation, at linear order, the uncertainties in f_R and Q are related to those in mass and angular momentum as

$$\frac{\Delta f_R}{f_R} = -\frac{\Delta M_{\text{rem}}}{M_{\text{rem}}} + \frac{f_2 f_3 (1 - \chi)^{f_3 - 1}}{f_1 + f_2 (1 - \chi)^{f_3}} \Delta \chi. \quad (2.7)$$

Similarly, from Eq. (2.5), we get

$$\Delta Q = \left(\frac{\Delta f_R}{f_R} - \frac{\Delta f_I}{f_I} \right) Q \quad (2.8)$$

$$= q_2 q_3 (1 - \chi)^{q_3 - 1} \Delta \chi. \quad (2.9)$$

In modified gravity theories, the final fate of binary mergers may not be a black hole. There are various possibilities of the modification of gravity. The most generic test for the deviation from general relativity would be just checking the consistency between the observed data and the predicted waveform based on general relativity. However, such a generic test will not be very sensitive. If we focus on some class of modification, we would be able to perform a much better test. Here, we assume that even if the gravity is modified the ringdown waveform is characterized by the set of (f_R, f_I) . For the same inspiral-merger waveform, which predicts the formation of a black hole with M and χ in GR, however, the values of (f_R, f_I) may be different. Under this assumption, one can test GR by comparing (f_R, f_I) predicted from the data in the inspiral-merger phase in GR with those directly extracted from the data in the ringdown phase. For this purpose, we wish to minimize the error in the determination of (f_R, f_I) from the data in the ringdown phase independent of the information contained in the inspiral-merger phase.

B. Mock data

The fundamental question we raise here is whether or not one can detect the deviation from the GR prediction, in case only the ringdown frequency is modified. If the breakdown of GR occurs only in the extremely strong gravity regime such as the region close to the BH event horizon, modification of gravity might be completely irrelevant to the evolution during the inspiral-merger phases. Even in such cases, the deviation from the GR prediction may show up in the ringdown waveform. This gives a good motivation to develop a method to identify the ringdown frequency without referring to the information from the inspiral-merger phases.

There are many proposals for the method to extract the ringdown frequency and its damping timescale. In order to compare the performance of various methods by a blind test, we construct some test data that have an artificially modified ringdown frequency.

We adopt the following strategy for preparing the data. We take the inspiral-merger waveform from the SXS gravitational waveform database [23,24] [there are also available catalogs for binary black hole (BBH) GWs in Refs. [25–28]], and the ringdown waveform modified from the GR case is merged. Then, noise is added to reproduce

the ideal LIGO noise curve [with the signal-to-noise ratio (SNR) = 20, 30, or 60]. In doing so, we focus on the fact that the time evolution of the amplitude and the frequency of the GR waveform is rather smooth if the spin precession can be neglected. Our basic assumption is that this smoothness is maintained even if we consider modification of the complex QNM frequencies. Then, the modified waveform cannot have a large variety.

We define a normalized time coordinate $x = (t - t_p)/M$, where t_p denotes the time that the GW amplitude has its peak and just modify the GW strain after the peak time. This is a reasonable assumption because, if the inspiral-merger parts are also modified, we can detect the deviation from GR even in the case when we cannot extract the QNM frequency from the gravitational wave data. Note that M is the initial total mass of the binary, and we will specify it later to generate the mock dataset. In the following, we take the simplification of considering only the $(\ell = 2, m = 2)$ GW mode.

To create the mock data, the total mass M is randomly selected from the range $50M_\odot - 70M_\odot$ with uniform probability. The parameters characterizing the ringdown waveform, f_R and f_I , are modified from the GR value within $\pm 30\%$ and $\pm 50\%$, respectively. Uniform probability distribution is assumed for both parameters. We present two independent ways to generate the mock data below.

1. Set A

In the case of set A, the modification is strictly limited to the time domain after the peak of the GW amplitude. First, as for the GW amplitude $A_{22} = r|h_{22}|/M$, we introduce the following fitting function:

$$A_{22}(t) = \frac{A_{22}^{\text{GR}}(t_p) + a_0 x + a_1 x^2}{1 - (M\omega_1 - a_0/A_{22}^{\text{GR}}(t_p))x + a_2 x^2} \times \exp(-M\omega_1 x), \quad (2.10)$$

where we have three fitting parameters a_0 , a_1 , and a_2 , which are chosen to reproduce the amplitude of the SXS waveform $A_{22}^{\text{GR}}(t)$ when the adjustable parameter $\omega_1 = f_I/(2\pi)$ is set to the GR value ω_1^{GR} calculated from the remnant BH mass and spin by using Refs. [22,29]. (In the following, the QNM frequency will often be written using angular frequency $\omega = 2\pi f$.) For example, for SXS:BBH:0174 [24], we have

$$\begin{aligned} a_0 &= 0.0183650, & a_1 &= 0.000998244, \\ a_2 &= 0.00184509, \end{aligned} \quad (2.11)$$

with $A_{22}^{\text{GR}}(t_p) = 0.286987$ and $M\omega_1^{\text{GR}} = 0.0815196$. The above fitting function is chosen such that the first derivative of the amplitude is zero at the peak ($x = 0$). By changing ω_1 , we can create mock data.

Second, as for the GW frequency $\omega_{22}(t)$, which is defined by the time derivative of the GW phase and supposed to be positive, we use the fitting function

$$M\omega_{22}(t) = (M\omega_{22}^{\text{GR}}(t_p) - M\omega_{\text{R}} + b_0x + b_1x^2 + b_2x^3) \times \exp\left[\frac{(b_0 + b_3)x}{M(\omega_{\text{R}} - \omega_{22}(t_p))}\right] + M\omega_{\text{R}}, \quad (2.12)$$

where $\omega^{\text{GR}}(t)$ is the frequency extracted from the phase of the numerically determined GR template. With this fitting function, the smoothness of the GW phase is C^2 at the peak time. The three fitting parameters are, again for SXS:BBH:0174,

$$\begin{aligned} b_0 &= -0.0507805, & b_1 &= -0.00276104, \\ b_2 &= -0.000479913, & b_3 &= -0.00492361, \end{aligned} \quad (2.13)$$

with $M\omega_{22}^{\text{GR}}(t_p) = 0.375598$. The mock data are created by changing the input $\omega_{\text{R}} = f_{\text{R}}/(2\pi)$ from the GR value calculated from the remnant BH mass and spin, e.g., $M\omega_{\text{R}}^{\text{GR}} = 0.582652$ for SXS:BBH:0174.

2. Set B

The modification of the second set is not strictly restricted to the time period after the peak of the amplitude. As another smooth interpolation, we adopt the following modified amplitude:

$$A_{22}(t) = \frac{A_{22}^{\text{GR}}(t)}{1 + e^{4M\omega_1^{\text{GR}}x}} + \frac{A_{22}^{\text{RD}}(t)}{1 + e^{-4M\omega_1^{\text{GR}}x}}, \quad (2.14)$$

with

$$A_{22}^{\text{RD}}(t) = \frac{\mathcal{A}_{22}}{1 + e^{-M\omega_1^{\text{GR}}x} + e^{M\omega_1^{\text{GR}}x}}, \quad (2.15)$$

and the overall amplitude \mathcal{A}_{22} determined so that the GR case fits well.

The frequency is also given in a similar simple manner by

$$\omega_{22}(t) = \frac{\omega_{22}^{\text{GR}}(t)}{1 + e^{4M\omega_1^{\text{GR}}x}} + \frac{\omega_{22}^{\text{RD}}(t)}{1 + e^{-4M\omega_1^{\text{GR}}x}}, \quad (2.16)$$

with the GR frequency $\omega_{22}^{\text{GR}}(t)$ and

$$\omega_{22}^{\text{RD}}(t) = \omega_{\text{R}}^{\text{GR}}(t_p) + \frac{\omega_{\text{R}} - \omega_{\text{R}}^{\text{GR}}(t_p)}{1 + e^{-2M\omega_1^{\text{GR}}x}}. \quad (2.17)$$

For generation of the set B mock data, we used SXS:BBH:0002, 0004, and 0007.

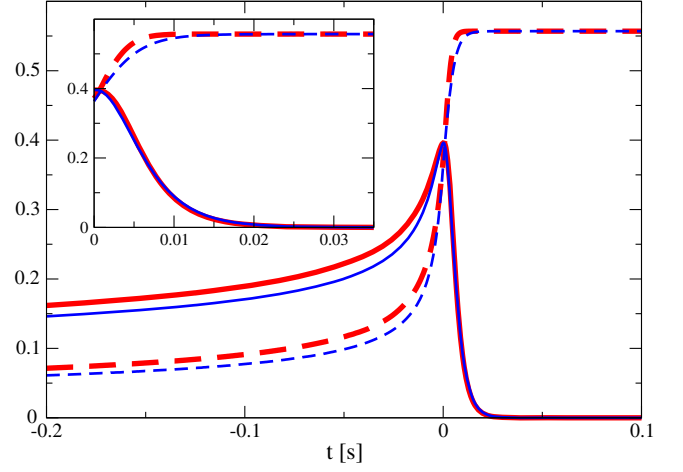


FIG. 1. Examples of sets A and B. (Inset) The ringdown part. Here, set A [(red) thick] with SXS:BBH:0174 and set B [(blue) thin] with SXS:BBH:0002 are shown. The solid lines denote the modified amplitude $A_{22}(t)$, and the dashed lines are the GW frequency $\omega_{22}(t)/(2\pi)$. The total mass is $M = 60M_{\odot}$, and the real and imaginary parts of the ringdown frequency are 300 and 40 Hz, respectively. The real frequency is obtained by multiplying by 538.609 Hz, and the real amplitude of set A is derived by dividing by 1.37903. The large difference in the inspiral phase is due to the difference of the binary parameters.

In Fig. 1, we show examples of sets A and B with a same ringdown frequency. It is noted that the binary parameters are different between SXS:BBH:0174 (set A) and SXS:BBH:0002 (set B) in Fig. 1.

III. VARIOUS METHODS FOR IDENTIFYING RINGDOWN MODE

A. Matched filtering with ringdown part

We perform the matched filtering analysis using simple damped sinusoidal templates, which are given by

$$\hat{h}(t) = \begin{cases} 0 & (t < t_0) \\ \frac{1}{N} e^{-\omega_1(t-t_0)} \cos[\omega_{\text{R}}(t-t_0) - \phi_0] & (t \geq t_0), \end{cases} \quad (3.1)$$

where t_0 and ϕ_0 are the starting time and the initial phase of the template, respectively. The normalization constant N is chosen so as to satisfy $(\hat{h}|\hat{h}) = 1$, where the inner product is defined by

$$(h_1|h_2) = 2 \int_0^{\infty} \frac{\tilde{h}_1^*(f)\tilde{h}_2(f) + \tilde{h}_1(f)\tilde{h}_2^*(f)}{S_n(f)} df. \quad (3.2)$$

Here, $S_n(f)$ is the noise spectral density, the Fourier transform of $h(t)$ is defined by $\tilde{h}(f) = \int dt e^{2\pi i f t} h(t)$, and $*$ denotes the complex conjugate. We consider to maximize the inner product between the GW data $s(t)$,

which contains the signal and the noise, and the template $h(t)$ over the parameters ω_R , ω_I , t_0 , and ϕ_0 . The SNR against the initial phase of the template can be maximized by rewriting the template in the following form:

$$h(t) = \frac{1}{N} (h_c \cos \phi_0 + h_s \sin \phi_0), \quad (3.3)$$

where

$$\begin{aligned} h_c &= e^{-\omega_I(t-t_0)} \cos[\omega_R(t-t_0)], \\ h_s &= e^{-\omega_I(t-t_0)} \sin[\omega_R(t-t_0)]. \end{aligned} \quad (3.4)$$

Then, the maximum of the SNR against the initial phase ϕ_0 can be given as [30]

$$\rho^2|_{\max \phi_0} = \frac{(s|\hat{h}_c)^2 + (s|\hat{h}_s)^2 - 2(s|\hat{h}_c)(s|\hat{h}_s)(\hat{h}_c|\hat{h}_s)}{1 - (\hat{h}_c|\hat{h}_s)^2}, \quad (3.5)$$

where

$$\hat{h}_c = \frac{h_c}{\sqrt{(h_c|h_c)}}, \quad \hat{h}_s = \frac{h_s}{\sqrt{(h_s|h_s)}}. \quad (3.6)$$

The phase ϕ_0 that gives the maximum ρ is given by

$$\tan \phi_0 = \frac{(h_c|h_s)(h|h_c) - (h_c|h_c)(h|h_s)}{(h_c|h_s)(h|h_s) - (h_s|h_s)(h|h_c)}. \quad (3.7)$$

Then, we are left with three parameters to explore. Since the best choice of the starting time of QNM is unknown, we vary t_0 from the merger time t_c to $t_c + \text{something}$. Then, we search for the best fit values of the parameters (f, Q) for each t_0 . Finally, we calculate the median values of $\{f(t_0), Q(t_0)\}$, which we regard as our estimate of the QNM frequency.

B. Matched filtering with both merger and ringdown parts

The plain matched filtering using the damped sinusoidal waveform, which was introduced in the preceding subsection, has difficulty in choosing the appropriate starting time t_0 . On one hand, if t_0 is chosen to be too early, we pick up lower frequency oscillations before the QNM starts to dominate. On the other hand, if t_0 is chosen to be too late, the signal has already become very faint and is buried in noise. Therefore, it is likely that this method is not the optimal method to determine the QNM frequency from the data.

The basic idea for the improvement of matched filtering is as discussed in Ref. [31]. If we know the modified ringdown waveform in advance, we can construct the best linear filter that produces the largest SNR by using it. As in the construction of our mock data in Sec. II A, here we also

assume that this smoothness is maintained even for the modified waveform. Then, the variety of the possible waveforms would be effectively limited well.

To obtain a better fit, one may think it would be necessary to introduce, at least, two more parameters in addition to (ω_R, ω_I) , i.e., the amplitude of QNM relative to that of the inspiral-merger phases and the transition rapidity to reach the final QNM frequency. It might be reasonable to perform the matched filtering using this generalized waveform including the inspiral-merger phases. To find the best fit parameter values in the four parameter space is doable. However, we adopt simplifications of neglecting these additional parameters here, in order to reduce the computational cost in the present analysis, leaving this possible extension to our future work. To reduce the impact of neglecting the relative amplitude of the QNM, we make use of the fact that the inspiral-merger parts are basically unchanged for all modified templates. Namely, we introduce the following sharp window function:

$$W(t) = \frac{1}{1 + e^{-50(t-t_c)\omega_I^{\text{GR}}}}, \quad (3.8)$$

to make the relative amplitude between the inspiral-merger phase and the ringdown phase almost irrelevant, instead of introducing one additional model parameter.

The procedure is summarized as follows. We first calculate the whitened signal and template multiplied by the window function, which are more explicitly defined by

$$\hat{s}(t) = W(t) \int df e^{-2\pi ift} \frac{\tilde{s}(f)}{\sqrt{S_n(f)}}, \quad (3.9)$$

and

$$\hat{h}(t) = NW(t) \int df e^{-2\pi ift} \frac{\tilde{h}(f)}{\sqrt{S_n(f)}}, \quad (3.10)$$

where N is the normalization factor that is determined to satisfy $(\hat{h}, \hat{h})^{(w)} = 1$, where $(*, *)^{(w)}$ is the inner product in Eq. (3.2), with $S_n(f)$ replaced with unity. After this preprocessing, the correlations between the data and templates are calculated as in the case of standard matched filtering, besides the point that the inner product $(*, *)^{(w)}$ is used instead of $(*, *)$. Here, we simply choose the phase that maximizes the signal-to-noise ratio ρ for each template, instead of marginalizing over these parameters. The origin of the time coordinate is not varied. To obtain the distribution of the parameters ω_R and ω_I , we simply used the probability given by $\propto \exp(\rho^2/2)$, which corresponds to the posterior distribution for the flat prior ansatz [32].

To perform the correlation analysis, we also need to specify a template waveform that includes the real and imaginary part of the QNM frequency as free parameters. To obtain the necessary template waveform, we shall use

the same prescription as set B that is used to generate half of the mock data. We understand that this makes the comparison for set B unfair, but one purpose of testing the improved matched filtering method arranged in this manner is to give a relevant standard to evaluate the efficiency of the other methods. The standard matched filtering using the damped sinusoidal wave as templates might be too naive to use it as the standard reference to assess the performance of the other methods. This improved matched filtering method is actually guaranteed to give the best linear filtering. Therefore, we think that the results obtained by this method offer a good reference to evaluate the performance of the other methods.

C. Hilbert-Huang transformation method

1. Basic idea

The Hilbert-Huang transform is a time-frequency analysis method [33], which is constructed with the aim to manipulate nonstationary and/or nonlinear systems. Some applications of the HHT to the data analysis of gravitational waves have been proposed [34–38]. The HHT is based on a signal analysis by the Hilbert transform. We describe the concept of the signal analysis by the Hilbert transform and its difficulty to be applied to real-world signals, and then explain how the HHT overcomes the difficulty.

Letting $\check{s}(t)$ be the Hilbert transform of a signal $s(t)$, it is defined by

$$\check{s}(t) = \frac{1}{\pi} \text{PV} \int dt' \frac{s(t')}{t-t'}, \quad (3.11)$$

where PV denotes the Cauchy principal value. The complex signal $z(t)$, which is defined by $z(t) = s(t) + i\check{s}(t)$, can be represented by the exponential form

$$z(t) = a(t)e^{i\phi(t)}, \quad (3.12)$$

where $a(t)$ and $\phi(t)$ are defined by

$$a(t) = \sqrt{s(t)^2 + \check{s}(t)^2}, \quad (3.13)$$

$$\phi(t) = \arctan\left(\frac{\check{s}(t)}{s(t)}\right). \quad (3.14)$$

Therefore,

$$s(t) = a(t) \cos \phi(t) \quad (3.15)$$

is established. Only when the signal $s(t)$ is monochromatic over short periods of time, $z(t)$ is an analytic signal of $s(t)$; in other words, the Fourier components of $z(t)$ are the same as $s(t)$ in the positive frequency range and zero in the negative frequency range [39], and then $a(t)$ and $\phi(t)$ are called the instantaneous amplitude (IA) and instantaneous

phase (IP) of $s(t)$, respectively. The monochromaticity of $s(t)$ over short periods of time means that $a(t)$ has only lower frequency components than $\cos \phi(t)$, or $a(t)$ and $\cos \phi(t)$ are the modulator and the carrier of the signal $s(t)$, respectively. In that case, the local mean $m(t)$ of $s(t)$, which is defined by

$$m(t) = \frac{u(t) + l(t)}{2}, \quad (3.16)$$

where $u(t)$ and $l(t)$ are the upper and lower envelopes of $s(t)$, respectively, is zero at any point. We call this feature the “zero mean.” An instantaneous frequency (IF) of $s(t)$ is defined by

$$f(t) = \frac{1}{2\pi} \frac{d\phi(t)}{dt}. \quad (3.17)$$

This analysis to estimate the IA and IF from a signal is called the Hilbert spectral analysis (HSA). The HSA has an advantage of higher resolution than the other time-frequency analyses, such as the short-time Fourier transform and the wavelet transform. However, it cannot be applied to most real-world signals, because they are basically composites of some components and are not monochromatic. Huang *et al.* [33] overcame the difficulty by combining a mode decomposition part with the HSA, and the method of combining them is the HHT.

Huang *et al.* developed a method to decompose the input data $x(t)$ into zero-mean components and a nonoscillatory component. They named the method the empirical mode decomposition (EMD) and also named the decomposed zero-mean components intrinsic mode functions (IMFs) of the input data. Algorithm 1 shows the procedure of the EMD, where $c_i(t)$ and $r(t)$ are the i th IMF and a non-oscillatory component of $x(t)$, respectively. The first step is forming the upper envelope $u_{i,j}(t)$ and the lower envelope $l_{i,j}(t)$, connecting the maxima and the minima of the data

Algorithm 1. Empirical mode decomposition.

```

1:  $i = 1$ ,  $x_1(t) = x(t)$ .
2: while  $x_i(t)$  contains oscillatory components do
3:    $j = 1$ ,  $x_{i,1}(t) = x_i(t)$ 
4:   while the local mean of  $x_{i,j}(t)$  is not zero do
5:      $u_{i,j}(t) =$  (the upper envelope of  $x_{i,j}(t)$ ).
6:      $l_{i,j}(t) =$  (the lower envelope of  $x_{i,j}(t)$ ).
7:      $m_{i,j}(t) = (u_{i,j}(t) + l_{i,j}(t))/2$ .
8:      $x_{i,(j+1)}(t) = x_{i,j}(t) - m_{i,j}(t)$ .
9:      $j = j + 1$ 
10:  end while
11:   $c_i(t) = x_{i,j}(t)$ 
12:   $x_{i+1}(t) = x_i(t) - c_i(t)$ .
13:   $i = i + 1$ .
14: end while
15:  $r(t) = x_i(t)$ 

```

by cubic splines. Then, the mean $m_{i,j}(t)$ of these envelope is subtracted from the input data to obtain the residual $x_{i,(j+1)}$. When the mean $m_{i,j}(t)$ becomes approximately zero after several iterations, $x_{i,j}$ is adopted as the IMF $c_i(t)$, since it can be considered to be zero mean. This criteria ϵ_e is a parameter of the EMD. After all oscillatory components are extracted, the residual $r(t)$ is a nonoscillatory component of $x(t)$. Letting N_{IMF} be the number of IMFs of $x(t)$, $x(t)$ is recovered by

$$x(t) = \sum_{n=1}^{N_{\text{IMF}}} c_n(t) + r(t). \quad (3.18)$$

IMFs, $c_1(t), c_2(t), \dots, c_{N_{\text{IMF}}}(t)$, are in order from the highest to lowest frequency components. After the above decomposition, the IA and IP of each IMF can be estimated by the HSA. Consequently, letting $a_n(t)$ and $\phi_n(t)$ be the IA and IP of n th IMF, the data can be expressed as

$$x(t) = \sum_{n=1}^{N_{\text{IMF}}} a_n(t) \cos \phi_n(t) + r(t). \quad (3.19)$$

In this study, we used the ensemble EMD (EEMD) as the mode decomposition method. In the beginning of the EEMD, N_e white noises $\{w^{(m)}(t)\}$ with the standard deviation being σ_e are created, and then the IMFs of the noise-added data $x^{(m)}(t) = x(t) + w^{(m)}(t)$ are calculated by the EMD,

$$x^{(m)}(t) = x(t) + w^{(m)}(t) \quad (3.20)$$

$$= \sum_{n=1}^{N_{\text{IMF}}} c_n^{(m)}(t) + r^{(m)}. \quad (3.21)$$

The IMFs of an input data $x(t)$ are estimated as the mean of the corresponding IMFs of $\{x^{(m)}(t)\}$,

$$c_n(t) = \frac{1}{N_e} \sum_{m=1}^{N_e} c_n^{(m)}(t). \quad (3.22)$$

The EEMD has two parameters (σ_e, ϵ_e): σ_e is a standard deviation of added white noise, and ϵ_e is a convergence-condition constant. The details of EEMD is shown in Refs. [37,40].

The basic concept of HHT for the QNM is as follows. If the QNM is perfectly extracted in the j th IMF, the IA and IP of the IMF must be expressed by

$$a_j(t) = Ae^{-(t-t_0)/\tau}, \quad (3.23)$$

$$\phi_j(t) = 2\pi f_R(t - t_0) + \phi_0. \quad (3.24)$$

Therefore, we can estimate the QNM frequency by fitting the IA and IP individually.

In reality, the IMF also contains other modes before the QNM starts, and noise components become dominant after the QNM is sufficiently damped. Equations (3.23) and (3.24) do not hold in the merger phase and the noise-dominant segment. Therefore, to estimate the QNM frequency with Eqs. (3.23) and (3.24), we need to estimate the segment where IA and IP most properly fits the equations. We constructed a method to estimate the segment, named the ‘‘QNM-dominant segment’’ (QDS), and the QNM frequency [38]. In the method, a bandpass filter, whose higher cutoff frequency is properly configured, will be applied as a preprocessing to extract a QNM into the first IMF.

2. QDS estimation

Here, we briefly describe how to estimate QDS [$\hat{n}_0, \hat{n}_0 + \hat{N}$]. Note that we represent discrete sequences with brackets, such as $t[n]$ and $a_1[n]$. Assuming the QNM is extracted in the first IMF, and its merger time $t[n_m]$ is known, we first search for the longest segment $[n_b, n_e]$ after n_m where the $a_1[n]$ decreases monotonically. For every possible subsegment $[n_0, n_0 + N]$ of $[n_b, n_e]$, where $N_{\text{min}} \leq N \leq n_e - n_b$, we calculate root-mean-squared errors $\text{RMSE}(n_0, N)$ of fitting $\ln a_1[n]$ with $bt[n] + c$,

$$\text{RMSE}(n_0, N) = \min_{b,c} \sqrt{\frac{1}{N} \sum_{n=n_0}^{n_0+N-1} (\ln a_1[n] - bt[n] - c)^2}. \quad (3.25)$$

We set N_{min} to five, the same configuration as in Ref. [38]. The optimal n_0 for each N is determined by

$$\hat{n}_0(N) = \underset{n_0}{\text{argmin}} \text{RMSE}(n_0, N), \quad (3.26)$$

and we define $e(N)$ as

$$e(N) = \text{RMSE}(\hat{n}_0(N), N). \quad (3.27)$$

The optimal N is determined as the transition point of a slope of the N - $e(N)$ plot,

$$\hat{N} = \underset{N}{\text{argmin}} [\text{Err}(N_{\text{min}}, N) + \text{Err}(N + 1, n_e - n_b)], \quad (3.28)$$

where $\text{Err}(N_1, N_2)$ is an error of the fitting $e(N)$ with $aN + b$,

$$\text{Err}(N_1, N_2) = \min_{a,b} \sqrt{\frac{\sum_{N=N_1}^{N_2} (e(N) - aN - b)^2}{N_2 - N_1}}. \quad (3.29)$$

Consequently, by letting $\hat{n}_0 = \hat{n}_0(\hat{N})$, the QDS $[\hat{n}_0, \hat{n}_0 + \hat{N}]$ is estimated. Then, the QNM frequency f_{qnm} can be

Algorithm 2. Estimation method of the QNM frequency with the HHT

Require: Strain $h[n]$ contains a BBH signal and merger time t_m is known

- 1: **for all** $(f_H, \epsilon_e, \sigma_e) \in F \otimes E \otimes \Sigma$ **do**
- 2: $h[n] \rightarrow h_{\text{filtered}}[n]$: apply a bandpass filter with cutoff frequency (f_L, f_H)
- 3: $h_{\text{filtered}}[n] \rightarrow a_1[n], \phi_1[n]$: apply the HHT with parameters (ϵ_e, σ_e) .
- 4: $[\hat{n}_0, \hat{n}_0 + \hat{N}]$: search the QNM-dominant segment (QDS) in $a_1[n]$
- 5: $\hat{f}_{\text{qnm}}(f_H, \hat{\epsilon}_e, \hat{\sigma}_e)$: estimate the QNM frequency by fitting $a_1[n], \phi_1[n]$ in the QDS
- 6: **end for**
- 7: $(\hat{f}_H, \hat{\epsilon}_e, \hat{\sigma}_e) = \underset{f_H, \epsilon_e, \sigma_e}{\text{argmin}} O(f_H, \hat{\epsilon}_e, \hat{\sigma}_e)$: select the set of parameters that optimizes an objective function O .
- 8: $\hat{f}_{\text{qnm}} = \hat{f}_{\text{qnm}}(\hat{f}_H, \hat{\epsilon}_e, \hat{\sigma}_e)$: the value of the selected combination is the estimated value of this method.

estimated by fitting the IA and IP with Eqs. (3.23) and (3.24) in the QDS.

3. Method

Here, we briefly explain the whole method to estimate QNM frequency from observed strain data $h[n]$. The outline of the method is described in Algorithm 2.

First, we have to determine candidate sets F , E , and Σ , which are sets of a higher cutoff frequency f_H of a bandpass filter, a convergence criteria ϵ_e of the EEMD, and a standard deviation σ_e of the added noise in the EEMD, respectively. In this study, we determined the sets as follows:

$$F = \{220, 225, 230, \dots, 500\} \text{ Hz}, \quad (3.30)$$

$$E = \{1 \times 10^{-1}, 4 \times 10^{-2}, 2 \times 10^{-2}, \dots, 1 \times 10^{-3}\}, \quad (3.31)$$

$$\Sigma = \{1 \times 10^{-3}, 4 \times 10^{-4}, 2 \times 10^{-4}, \dots, 1 \times 10^{-5}\}, \quad (3.32)$$

and f_L is set to 20 Hz. For each parameter candidate $(f_H, \epsilon_e, \sigma_e)$, a series of processing, including a bandpass filter with cutoff frequency (f_L, f_H) , the HHT, and the search of QDS, is applied to the input strain data $h[n]$. After that, the optimal set of the parameters will be selected under an objective function O . We used the slope of the linear function obtained by fitting $f_1[n]$ in the range of the searched QDS as the objective function O , since the IF must be flat in the QDS if a QNM is properly extracted.

D. Autoregressive modeling method

1. Basic idea

The autoregressive method is well-known time-sequence analysis method that is used in, e.g., acoustic signal processing [41]. Suppose we have the signal data of a segment, $x_n = x(n\Delta t)$, ($n = 1, 2, \dots, N$). The main idea is to express the signal x_n with its previous $M (< N)$ data,

$$x_n = \sum_{j=1}^M a_j x_{n-j} + \epsilon, \quad (3.33)$$

where a_j and M are the coefficients and the order of the AR model, respectively, and ϵ is the residual treated as white noise in this modeling. If the data x_n are damped sinusoidal waves without noise, then we analytically can express x_n with $M = 2$. Even when the data include noise, we expect to extract the actual signals by tuning N and M . There are various methods proposed to determine a_j and M . In this article, we present the results using the Burg method for a_j and the final prediction error (FPE) method for M . The details and other trials are in Ref. [42].

Once the model (3.33) is fixed, we then reconstruct the wave signal from Eq. (3.33) and analyze it. By setting $z(f) = e^{2\pi i f \Delta t}$, the power spectrum of the wave signal can be expressed as

$$p(f) = \sigma^2 \left| 1 - \sum_{j=1}^M a_j z^{-j} \right|^{-2}, \quad (3.34)$$

where σ is the variance of ϵ . The resolution of frequency in Eq. (3.34) is not limited by the length of the original dataset, so that AR method is expected to identify signal frequency more precisely than the standard (short-) Fourier decomposition.

From Eq. (3.33), the (local) maximums of the spectrum $p(f)$ are given at

$$F(z) = 1 - \sum_{j=1}^M a_j z^{-j} \approx 0. \quad (3.35)$$

This is an M th-order polynomial equation. The solutions of the characteristic equation, $F(z) = 0$, also express the fundamental modes that consist of the data segment. By interpreting the M solutions as $z_k = e^{2\pi i f_k \Delta t}$ ($k = 1, \dots, M$), we get the fundamental frequencies from the real part of f_k and damping rates from the imaginary part of f_k . [Actually, $|z_k| \leq 1$ is expected for the expression (3.33) to be stable.] Therefore, the AR method can determine the frequencies and damping rates of quasinormal modes from the data themselves.

2. Method

We divided the given mock data into segments of the length of $\Delta T = 1/128$ sec ($N = 32$). The neighboring segments are largely overlapping shifted only by 4 points. For each segment, we modeled the data with Eq. (3.33) with Burg and FPE methods. Normally M falls into the range 2–5.

We then get the power spectrum $p(f)$ from Eq. (3.34) at each segment and locate its local maximums f_1, f_2, \dots with their one-sigma widths. We also solve Eq. (3.35) at each segment (which is at most a 5th-order polynomial equation) and identify the solution z_k of which the real part of the frequency is the closest to f_1, f_2, \dots .

We list these solutions z_k of each segment and check whether they remain almost unchanged over several segments. If the successive segments have a common frequency mode within one-sigma width, then we make a short list as the candidates for ringdown modes.

We see sometimes a segment is full of noises and shows quite different numbers from neighboring segments. In most cases, however, after the time of a black hole merger, we can identify one common frequency that overlaps within one-sigma width for several data segments.

E. Neural network method

1. Convolutional neural network

In this challenge, we use a “convolutional neural network” (CNN), which can extract local patterns of the data. CNNs are often used for the image recognition and we expect CNNs can be applied to the GW data analysis [43]. We try various CNNs that have different structure, layers, neurons, and filters. The final configuration of the CNN that is used here is shown in Table I.

In general, the input and output data of a convolutional layer have multichannels. The data with multichannels have multivalued in each pixel (e.g., RGB components of images). In a convolutional layer, convolutions of the data containing L channels and the L' filters h ,

$$z'_{i,l'} = \sum_{l=1}^L \sum_{p=1}^H z_{i+p,l} h_{p,l'}^l + b_{i,l'}, \quad (3.36)$$

are calculated to extract the local patterns. Here, z and z' are the input and output vectors of the layer, respectively. The number and the length of the filters, L' and H , are fixed before training and the coefficients h and biases b are optimized in the training procedure. In this work, we use four convolutional layers. The lengths of the filters are 32, 16, 8, and 8, and the numbers of the filters are 64, 128, 256, and 512, respectively.

A pooling layer, often placed after a convolutional layer, compresses information, combining a few pixels into one pixel. In this work, we use the max pooling,

$$z'_i = \max_{k=1, \dots, p} z_{si+k}. \quad (3.37)$$

TABLE I. The configuration of the CNN we use. (x, y) means that the data each layer returns have x points and y channels. Each input data have only one channel, h_+ , which are composed of 512 points. The “Flatten” layer reshapes two-dimensional data to one-dimensional data.

Layer	Dimension
Input	(512, 1)
Convolution	(481, 64)
Pooling	(240, 64)
ReLU	(240, 64)
Convolution	(225, 128)
Pooling	(112, 128)
ReLU	(112, 128)
Convolution	(105, 256)
Pooling	(52, 256)
ReLU	(52, 256)
Convolution	(45, 512)
Pooling	(22, 512)
ReLU	(22, 512)
Flatten	16×512
Dense	256
ReLU	256
Dense	2
Output	2

Here, s is the stride and p is the size of the pooling filter. We set $s = p = 2$.

In most cases, dense layers, which are linear transformations,

$$z'_i = \sum_{j=1}^N w_{ij} z_j + b_i, \quad (3.38)$$

with N being the number of input values, are located after convolutional layers. The weights w and biases b are optimized in training.

An activation function plays an important role to carry out nonlinear transformations. In this work, we use the rectified linear unit (ReLU),

$$z' = h(z) = \max(z, 0), \quad (3.39)$$

as activation functions.

For an accurate estimation, weights and biases in dense layers and filters in the convolutional layers need to be optimized using training data. In the case of supervised learning, the training data include a pair of input data and a target vector. In our work, the input data are the time series of gravitational wave signals with noise and the target vector is composed of the QNM frequency $(f_R^{(inj)}, f_I^{(inj)})$. For an input, the neural network returns an estimated vector $(f_R^{(pred)}, f_I^{(pred)})$ and compares it with a target vector. The loss function is computed to evaluate the error between the estimated and target vectors. In batch learning, a group of data, called a “batch” with its size N_b fixed before training,

is used to define the loss function. As the loss function, we adopt the mean relative error,

$$J = \frac{1}{N_b} \sum_{n=1}^{N_b} \sum_{A \in \{R,I\}} \frac{|f_{n,A}^{(\text{pred})} - f_{n,A}^{(\text{inj})}|}{f_{n,A}^{(\text{inj})}}. \quad (3.40)$$

We set $N_b = 64$. As an optimization method, we use the Adam [44]. The hierarchical training, proposed in Ref. [43], is adopted. The training starts from using the injected data, whose peak SNR [45] is 20.0, and gradually decreasing the peak SNR. At the final stage of training, we use the signal of which the peak SNR ranges from 10.0 to 3.0.

We use PYTORCH software [46]. For accelerating learning with NVIDIA GPU, we employ the CUDA deep neural network library [47].

2. Training dataset

First, we construct the template bank for the training using the modified waveform, which is based on the same method as Eqs. (2.14) and (2.16). For the template bank, f_R and f_I are uniformly placed in the range 209–378 and 23–69 Hz. The template bank contains 21×21 waveforms.

Next, each waveform is whitened using Advanced LIGO's design sensitivity (aLIGOZeroDetHighPower). From each signal, we pick up the segment that consists of 512 points starting from the coalescence time, and these whitened waveforms are injected into the white Gaussian noises. The realization of noises is varied for each training step in order to prevent the neural network from being overfitted with some particular noise patterns. Finally, we normalize each segment to have mean 0.0 and variance 1.0.

IV. COMPARISON AND SUMMARY

A. Overview

We prepare 120 mock data in total by using the method described in Sec. II B. Half of them are generated using Eqs. (2.10) and (2.12), and the others are generated using Eqs. (2.14) and (2.16). We refer to the former as set A and the latter as set B. For both sets, we generated 20 mock data, respectively, with overall SNR, $\rho_{\text{all}} = 60, 30$, and 20. The SNR for the ringdown part ρ_{rd} turned out to be roughly $1/5 \sim 1/3$ of ρ_{all} . We listed the details of a part of the mock data in Table II. We calculated ρ_{rd} by the standard inner product for the injected waveform after the peak of the amplitude without noise.

The five challenging groups received 120 data files of $h(t)$, together with rough information of the merger time t_0 for each of the data, but not with the frequency of the injected ringdown waveform, $(f_R^{(\text{inj})}, f_I^{(\text{inj})})$. The mock data themselves are provided with both the $+$ mode and \times mode, but this time we used only the $+$ mode. Since $(f_R^{(\text{inj})}, f_I^{(\text{inj})})$ are randomly shifted from the values in

TABLE II. A partial list of mock data. Set A was generated using Eqs. (2.10) and (2.12), while set B was from Eqs. (2.14) and (2.16). The overall SNR ρ_{all} , SNR of the ringdown part ρ_{rd} , and injected value of the ringdown waveform $(f_R^{(\text{inj})}, f_I^{(\text{inj})})$ are shown.

Data	SNR		Injected	
	ρ_{all}	ρ_{rd}	$f_R^{(\text{inj})}$	$f_I^{(\text{inj})}$
A-01	60.0	11.87	260.68	44.58
A-02	60.0	12.82	345.16	50.49
A-03	60.0	13.31	382.53	32.58
A-04	60.0	12.49	284.18	44.73
A-05	60.0	14.25	346.20	23.07
A-06	30.0	6.18	272.85	33.40
A-07	30.0	6.07	272.85	44.54
A-08	30.0	6.05	301.89	42.24
A-09	30.0	6.75	324.60	27.25
A-10	30.0	6.08	282.55	37.45
A-11	20.0	4.59	314.24	30.58
A-12	20.0	3.85	382.10	48.60
A-13	20.0	4.01	249.36	47.97
A-14	20.0	3.98	299.32	41.88
A-15	20.0	4.09	319.42	31.55
B-01	60.0	15.93	352.56	36.20
B-02	60.0	15.62	210.78	42.77
B-03	60.0	15.31	258.83	48.42
B-04	60.0	18.34	271.13	25.40
B-05	60.0	15.92	291.99	34.20
B-06	30.0	8.55	411.57	29.48
B-07	30.0	6.78	295.78	59.38
B-08	30.0	7.03	312.39	59.24
B-09	30.0	7.68	198.34	57.91
B-10	30.0	7.81	323.32	37.86
B-11	20.0	5.79	208.80	39.75
B-12	20.0	5.76	246.66	27.85
B-13	20.0	4.46	323.71	62.51
B-14	20.0	5.62	215.15	33.15
B-15	20.0	5.99	335.20	25.11

TABLE III. We show the values of $\overline{\delta \log f_R}$, $\sigma(f_R)$, $\overline{\delta \log f_I}$, and $\sigma(f_I)$ for various methods. The results limited to set A are given on the first law of each method, while those limited to set B are on the second.

		$\overline{\delta \log f_R}(\%)$	$\sigma(f_R)(\%)$	$\overline{\delta \log f_I}(\%)$	$\sigma(f_I)(\%)$
MF-R	A	-12.88	28.36	-71.51	97.79
	B	-0.82	27.53	-46.11	75.48
MF-MR	A	6.25	17.27	-12.62	37.9
	B	2.47	10.41	7.18	27.61
HHT	A	-13.38	21.91	-44.11	61.58
	B	-8.08	19.81	-28.78	49.61
AR	A	0.2	9.93	4.88	38.75
	B	1.91	8.57	6.2	34.64
NN	A	-6.64	16.48	-15.23	33.96
	B	-6.65	11.97	9.96	23.76

general relativity, the challengers cannot use the information of inspiral part for their estimation of (f_R, f_I) . Some methods (MF-R/MR, AR) can derive the estimation value (f_R, f_I) with their error bars, while some (HHT, NN) cannot. Therefore, we simply compare the results of the estimated (central) values.

B. Results and comparison

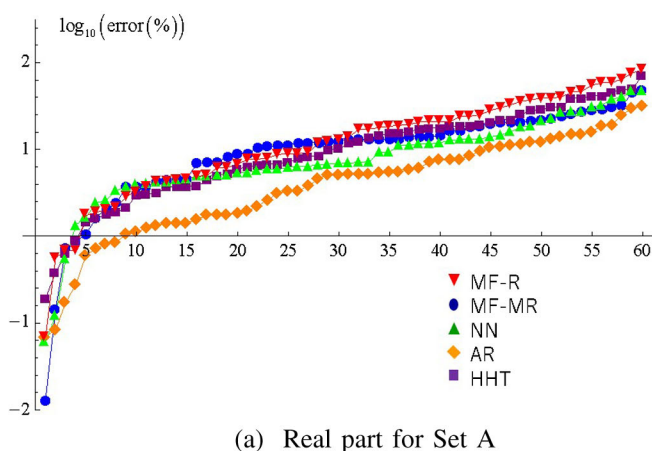
For 120 data, each challenging group handed in (f_R, f_I) as the result of their blind analyses. In order to compare five methods, we introduce the logarithmic average and variance defined by

$$\begin{aligned} \overline{\delta \log Q} &= \frac{1}{N} \sum_{n=1}^N \left(\log \frac{Q_n^{(\text{estimate})}}{Q_n^{(\text{inj})}} \right), \\ \sigma(Q) &= \left[\frac{1}{N} \sum_{n=1}^N \left(\log \frac{Q_n^{(\text{estimate})}}{Q_n^{(\text{inj})}} \right)^2 \right]^{1/2}, \end{aligned} \quad (4.1)$$

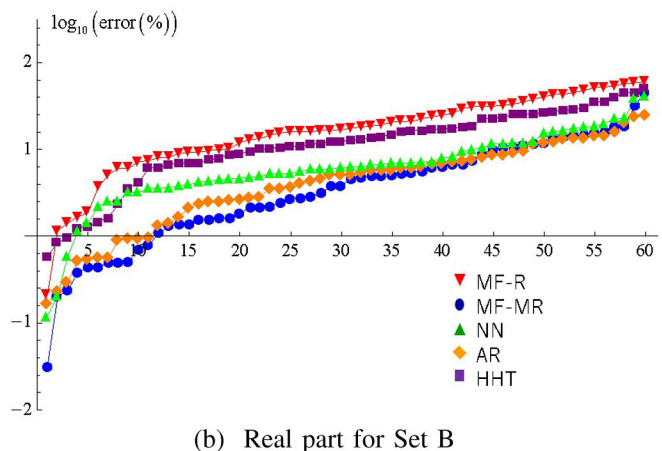
as indicators of the bias and the average magnitude of the parameter estimation error, where $Q_n^{(\text{estimate})}$ is the estimated value of the quantity Q for the n th data and $Q_n^{(\text{inj})}$ is the corresponding injected values. In Table III, we show the values of $\overline{\delta \log f_R}$, $\sigma(f_R)$, $\overline{\delta \log f_I}$, and $\sigma(f_I)$ for the methods we tried. We show the results limited to set A on the first law and those limited to set B on the second law.

We should recall that, in the actual implementation of the MF-MR described in Sec. III B, we adopt the same modified template that is used to generate set B mock data. Also, the NN method introduced in Sec. III E uses the template bank generated in the same way as set B mock data to train the network.

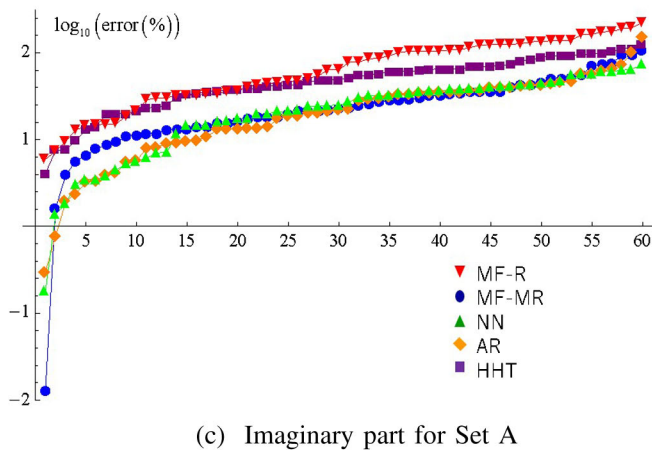
The error of MF-R using the simple damped sinusoidal waveform is relatively large, as expected. In fact, the error of the estimates of f_R and f_I is the largest among the five methods. The results of the HHT method are not so good, either. At least, the current way of using MF-R or HHT for the estimate of imaginary part of QNM frequency does not seem to be competitive compared with the other methods.



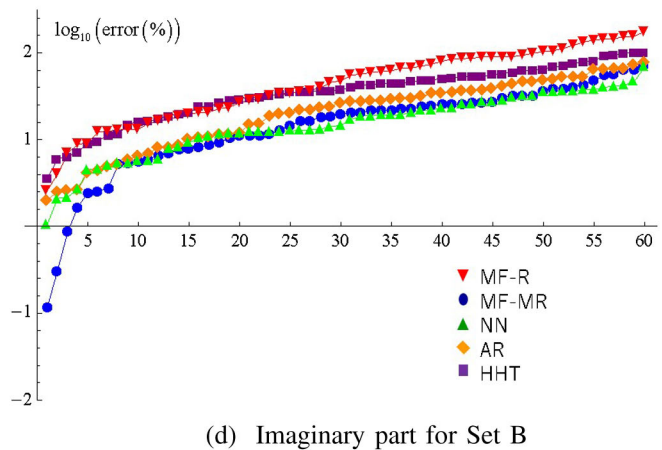
(a) Real part for Set A



(b) Real part for Set B



(c) Imaginary part for Set A



(d) Imaginary part for Set B

FIG. 2. Plots of the base 10 logarithm of the error in the estimate for all test data [(a) and (b) for the real part for sets A and B, respectively, and (c) and (d) for the imaginary part for sets A and B, respectively]. The data number is sorted for each method in ascending order of the magnitude of the error.

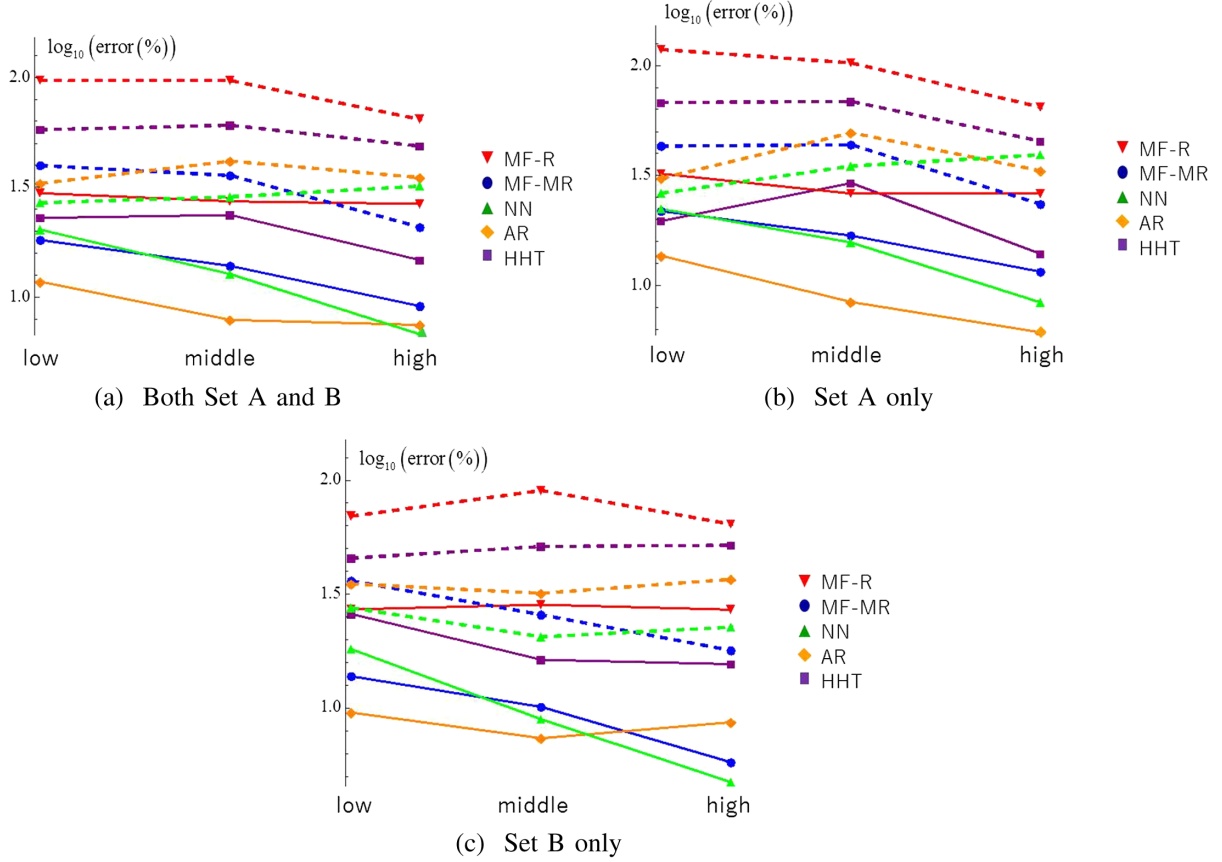


FIG. 3. The root-mean-square error in percent of each method for three levels of SNR [(a) for both sets A and B, (b) for only set A, and (c) for only set B]. The solid and dashed lines represent the real and imaginary parts, respectively.

The performances of the other three methods, i.e., MF-MR, AR, and NN methods, are almost comparable for the imaginary part, while the determination of the real part by AR looks better than the other two methods. Here, we should recall that the comparison with MF-MR and NN is not fair in the case of set B mock data, since their base templates are constructed from set B data. The results of MF-MR and NN are better for set B, as expected.

The variance might be determined by a small number of data with a large error. To check if that is the case or not, we give plots of the absolute magnitude of the error $|\log(Q_n^{\text{estimate}}/Q_n^{\text{inj}})|$ sorted in ascending order for each method in Fig. 2. Although the number of data are small, these figures tell us that the tendencies mentioned above are not the ones that hold only for the data with a large error.

To show how the errors depend on SNR, we present several plots of the averaged values within each level of SNR: high, middle, and low, i.e., $\rho_{\text{all}} = 60, 30, \text{ and } 20$. The variances of the differences $\delta \log f_R = \log f_R - \log f_R^{(\text{inj})}$ and $\delta \log f_I = \log f_I - \log f_I^{(\text{inj})}$ are shown in Fig. 3, respectively. The solid lines denote the results for the real part while the dashed lines are those for the imaginary part. The estimations of f_I are generally about 0.5 order worse than those of f_R . This tells us the difficulty of identifying the

damping rate. As expected, the differences are smaller for larger ρ_{all} , with some exceptions. The main message we can read from Fig. 3 combined with Table II is that we would be able to estimate f_R within 7% (8%) from the injected value for the data $\rho_{\text{rd}} \sim 15$ (8), if we adopt an appropriate method. On the other hand, the estimate of f_I has an error at least of $O(30\%)$ even for the data with $\rho_{\text{rd}} \sim 15$.

The averages of $\delta \log f_R$ and $\delta \log f_I$ are also shown in Fig. 4. For all five methods, we see the estimated values of f_R are roughly distributed around the injected one $f_R^{(\text{inj})}$, while there are some tendencies that $f_I^{(\text{inj})}$ is over- or underestimated, depending on the method. These results would be suggestive in the interpretation of the future application of each method to real data.

C. Error estimate

MF-MR and AR methods give the error estimates as explained in Sec. III. The consistency of these error estimates is briefly checked below.

In the case of the MF-MR method for set B data, the expected result is obtained. Namely, there are 120 guesses in the present test (60 real parts and 60 imaginary parts). The 90% confidence interval is given by cutting 5% probability regions on both small and large value sides.

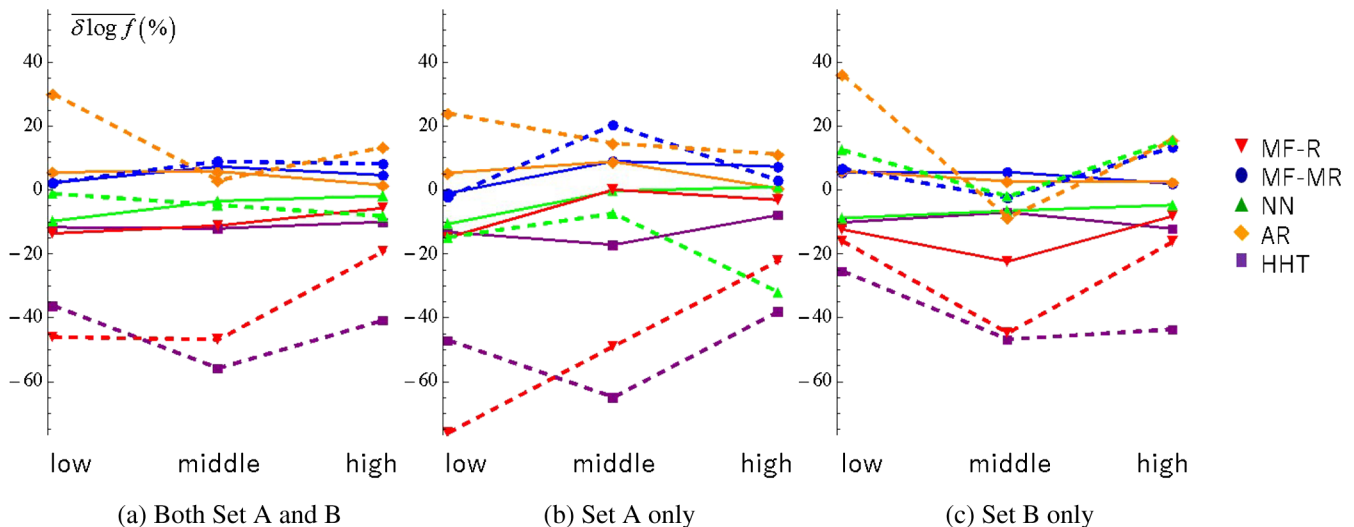


FIG. 4. The averaged error in percent of each method for three levels of SNR [(a) for both sets A and B, (b) for only set A, and (c) for only set B]. The solid and dashed lines represent the real and imaginary parts, respectively.

This estimate of the confidence interval just takes into account the statistical error. The true value fell outside of the confidence interval 27 times out of 120. This is slightly worse than the expectation. The estimate of the confidence interval may need modification. For set A data, this happened 45 times, which means that the contribution of the systematic bias is significantly large.

For the AR method, the true value becomes outside the 90% confidence interval 21 times out of 120 guesses for the imaginary part, while it happened 51 times for the real part.

V. CONCLUDING REMARKS

We implemented five methods for extracting ringdown waves solely and tested them with mock data by a method of “blind analysis.”

Comparison tells us that the AR method, which can pick up the frequency of ringdown wave f_R with 10% root-mean-square difference from the injected one for the SNR of the ringdown part greater than 7 or so, showed the best performance in determining the real part. The AR method is superseded by the NN or MF-MR method for set B data with high SNR of the ringdown part greater than 12 or so. The same template as set B data is used as the training data for the NN method and as the template to be matched for the MF-MR method. On the other hand, the imaginary part of the frequency f_I (related to the damping period) is rather difficult to determine, and AR, NN, and MF-MR methods showed comparable performance. The data tell us that the root-mean-square difference of f_I from the injected one for high SNR data can be less than about 30%, although the result would apply only in modifications of the ringdown waveform limited to the one smoothly connected to the merger phase. We believe that the possibility and the limitation of independent estimation of the ringdown mode

was shown in this paper, and this opens a way of testing gravity theories.

When the error circles derived by using some combination of several methods are overlapping, we might be able to more confidently claim that the QNM frequency is determined by the observational data. However, currently, only two of our analysis methods (MF-MR, AR) reported error circles, and the estimated error circles also contain some errors. Once we have various methods whose error estimate is reliable, there might be a possibility to combine the estimates properly.

Through the mock-data challenges, we also learned the directions for further improvements of each method.

- (i) The MF methods do not have much room for further improvement. As for MF-MR, one possible extension is to adopt a little wider class of templates that depend on parameters other than the QNM frequency. However, the preliminary trial calculations suggest that the extension in this direction will not be so successful.
- (ii) The AR method, presented here, used the Burg method for fitting data and the final prediction error method for fixing the length of data sequence. We think that it will be interesting to compare with similar but slightly different approaches, such as those proposed by Berti *et al.* [14].
- (iii) In the HHT method, there exists the mode-splitting problem of the EMD [48]. We are planning to resolve the problem by taking into account the sparsity in the frequency domain to the EMD. It may improve the accuracy of the extraction of a QNM since the instantaneous frequency of the QNM is constant.
- (iv) First, the neural network is trained with waveforms generated by the same method as set B. So, the results for set A seem to contain bias in the high SNR

regime. The improvement of the training algorithm or preparing the dataset will reduce the bias. Second, the NN method can give only the central value for the current estimation. We need to find a method to estimate the prediction errors.

After implementations of such improvements, we are planning to apply our methods to the real GW data, to discuss the validity of general relativity.

ACKNOWLEDGMENTS

This research made use of data generated by the Simulating eXtreme Spacetimes. This work was supported

by JSPS KAKENHI Grant No. JP17H06358 (and also JP17H06357), *A01: Testing gravity theories using gravitational waves*, as a part of the innovative research area, “Gravitational wave physics and astronomy: Genesis”. H. N. acknowledges support from JSPS KAKENHI Grant No. JP16K05347. The work of T. N. was also supported in part by a Grant-in-Aid for JSPS Research Fellows. H. S. acknowledges also support from JSPS KAKENHI Grants No. JP18K03630 and No. 19H01901. H. T. acknowledges support from JSPS KAKENHI Grant No. JP17K05437. T. T. acknowledges support from JSPS KAKENHI Grants No. JP26287044 and No. JP15H02087.

-
- [1] B. P. Abbott *et al.* (LIGO Scientific and Virgo Collaborations), *Phys. Rev. Lett.* **116**, 061102 (2016).
- [2] B. P. Abbott *et al.* (LIGO Scientific and Virgo Collaborations), *Phys. Rev. Lett.* **116**, 241103 (2016).
- [3] B. P. Abbott *et al.* (LIGO Scientific and Virgo Collaborations), *Phys. Rev. Lett.* **118**, 221101 (2017).
- [4] B. P. Abbott *et al.* (LIGO Scientific and Virgo Collaborations), *Astrophys. J.* **851**, L35 (2017).
- [5] B. P. Abbott *et al.* (LIGO Scientific and Virgo Collaborations), *Phys. Rev. Lett.* **119**, 141101 (2017).
- [6] B. P. Abbott *et al.* (LIGO Scientific and Virgo Collaborations), *Phys. Rev. Lett.* **119**, 161101 (2017).
- [7] B. P. Abbott *et al.* (LIGO Scientific and Virgo Collaborations), [arXiv:1811.12907](https://arxiv.org/abs/1811.12907).
- [8] B. P. Abbott *et al.* (LIGO Scientific and Virgo Collaborations), [arXiv:1811.12940](https://arxiv.org/abs/1811.12940).
- [9] T. Akutsu *et al.* (KAGRA Collaboration), *Nat. Astron.* **3**, 35 (2019).
- [10] T. Akutsu *et al.* (KAGRA Collaboration), [arXiv:1901.03569](https://arxiv.org/abs/1901.03569) [Classical Quantum Gravity (to be published)].
- [11] B. P. Abbott *et al.* (LIGO Scientific, Virgo, and KAGRA Collaborations), *Living Rev. Relativity* **21**, 3 (2018).
- [12] C. M. Will, *Living Rev. Relativity* **17**, 4 (2014).
- [13] E. Berti, J. Cardoso, V. Cardoso, and M. Cavagliá, *Phys. Rev. D* **76**, 104044 (2007).
- [14] E. Berti, V. Cardoso, J. A. González, and U. Sperhake, *Phys. Rev. D* **75**, 124017 (2007).
- [15] T. Damour and A. Nagar, *Phys. Rev. D* **90**, 024054 (2014).
- [16] L. London, D. Shoemaker, and J. Healy, *Phys. Rev. D* **90**, 124032 (2014).
- [17] E. Berti, V. Cardoso, and A. O. Starinets, *Classical Quantum Gravity* **26**, 163001 (2009).
- [18] V. Cardoso and L. Gualtieri, *Classical Quantum Gravity* **33**, 174001 (2016).
- [19] E. Berti, K. Yagi, H. Yang, and N. Yunes, *Gen. Relativ. Gravit.* **50**, 49 (2018).
- [20] https://gw-genesis.scphys.kyoto-u.ac.jp/ilias/goto_root_lm_1287.html.
- [21] H. Nakano, T. Tanaka, and T. Nakamura, *Phys. Rev. D* **92**, 064003 (2015).
- [22] E. Berti, V. Cardoso, and C. M. Will, *Phys. Rev. D* **73**, 064030 (2006).
- [23] A. H. Mroue *et al.*, *Phys. Rev. Lett.* **111**, 241104 (2013).
- [24] <https://www.black-holes.org/waveforms/>.
- [25] K. Jani, J. Healy, J. A. Clark, L. London, P. Laguna, and D. Shoemaker, *Classical Quantum Gravity* **33**, 204001 (2016).
- [26] <http://www.einstein.gatech.edu/catalog/>.
- [27] J. Healy, C. O. Lousto, Y. Zlochower, and M. Campanelli, *Classical Quantum Gravity* **34**, 224001 (2017).
- [28] <https://ccrg.rit.edu/~RITCatalog/>.
- [29] <https://pages.jh.edu/~eberti2/ringdown/>.
- [30] H. Nakano, H. Takahashi, H. Tagoshi, and M. Sasaki, *Phys. Rev. D* **68**, 102003 (2003); *Prog. Theor. Phys.* **111**, 781 (2004).
- [31] W. Del Pozzo and A. Nagar, *Phys. Rev. D* **95**, 124034 (2017).
- [32] The Likelihood function would be defined by the probability of the model parameters θ when data D is provided, $P(\theta|D)$. Using the Bayes theorem, we can write $P(\theta|D)$ as $P(\theta|D) = \frac{P(D|\theta)P(\theta)}{P(D)}$. When we assume a flat prior distribution, i.e., $P(\theta) = \text{constant}$, we have $P(\theta|D) \propto P(D|\theta)$. The probability that data D is described by a normalized template $\hat{h}(\theta)$ and the noise n as $\rho\hat{h} + n$ would be given by $P(D|\rho, \theta) \propto \exp[-(n|n)/2] = \exp[-(D - \rho\hat{h}(\theta)|D - \rho\hat{h}(\theta))/2]$. Marginalizing this probability with respect to ρ , we find $P(D|\theta) \propto \exp[-(D|\hat{h}(\theta))^2/2]$. When we have some unfocused extra parameters, we need to marginalize the probability over these extra parameters. Here the coalescence time and the overall phase are such parameters. For the coalescence time, we just adopt the maximum value, in place of the marginalization, which we expect will not cause any significant error.
- [33] N. E. Huang, Z. Shen, S. R. Long, M. C. Wu, H. H. Shih, Q. Zheng, N. C. Yen, C. C. Tung, and H. H. Liu, *Proc. R. Soc. A* **454**, 903 (1998).
- [34] J. B. Camp, J. K. Cannizzo, and K. Numata, *Phys. Rev. D* **75**, 061101 (2007).
- [35] A. Stroerer, J. K. Cannizzo, J. B. Camp, and N. Gagarin, *Phys. Rev. D* **79**, 124022 (2009).

- [36] H. Takahashi, K. Oohara, M. Kaneyama, Y. Hiranuma, and J. B. Camp, *Adv. Adapt. Data Anal.* **05**, 1350010 (2013).
- [37] M. Kaneyama, K. Oohara, H. Takahashi, Y. Sekiguchi, H. Tagoshi, and M. Shibata, *Phys. Rev. D* **93**, 123010 (2016).
- [38] K. Sakai, K. Oohara, H. Nakano, M. Kaneyama, and H. Takahashi, *Phys. Rev. D* **96**, 044047 (2017).
- [39] L. Cohen, *Time Frequency Analysis: Theory and Applications* (Prentice-Hall, Englewood Cliffs, NJ, 1995).
- [40] Z. Wu and N. E. Huang, *Adv. Adapt. Data Anal.* **01**, 1 (2009).
- [41] S. L. Marple, Jr, *Digital Spectral Analysis* (Prentice-Hall, Englewood Cliffs, NJ, 1987).
- [42] H. Shinkai, (in preparation).
- [43] D. George and E. A. Huerta, *Phys. Rev. D* **97**, 044039 (2018).
- [44] D. P. Kingma and J. Ba, [arXiv:1412.6980](https://arxiv.org/abs/1412.6980).
- [45] The definition of peak SNR is $(\text{peak SNR}) = (\text{maximum amplitude of template}) / (\text{variance of noise})$.
- [46] P. Adam *et al.*, in *Proceedings of the NIPS 2017 Workshop* (2017), <https://openreview.net/forum?id=BJJsrmfCZ>.
- [47] S. Chetlur *et al.*, [arXiv:1410.0759](https://arxiv.org/abs/1410.0759).
- [48] J. Yeh, J. Shieh, and N. E. Huang, *Adv. Adapt. Data Anal.* **02**, 135 (2010).